Geochemical Perspectives Letters

Inferred pyrite growth via the particle attachment pathway in the presence of trace metals

J.M. Domingos, E. Runge, C. Dreher, T.-H. Chiu, J. Shuster, S. Fischer, A. Kappler, J.-P. Duda, J. Xu, M. Mansor

Supplementary Information

The Supplementary Information includes:

- Materials and Methods
- SI Discussion
- Tables S-1 to S-4
- Figure S-1 to S-3
- Supplementary Information References

Materials and Methods

Pyrite synthesis

Pyrite was synthesised using a modified method detailed in Mansor and Fantle (2019). Two sets of experiments were performed – one at the University of Texas at El Paso in 2019, and another at the University of Tuebingen in 2022. Differences between the two experimental sets are detailed in Table S-2. For both experimental sets, the following reagents were prepared in an anoxic glovebox: (1) 3 mM iron (Fe^{2+}) solution in 20 mM NaCl, (2) 180 mM sulphide solution, freshly prepared by dissolving $Na_2S•9H_2O$ in anoxic MQ H_2O on the same day of the experiment, (3) 1 M HEPES buffer, pH pre-adjusted to 7 with NaOH and (4) trace metal solutions (Co/Cu/Mo/Ni/Zn) either at 2 mM or 2 µM. Different trace metal concentrations were used to achieve a final metal:Fe ratio of either $1:10^2$ (*high-metal* experiments) or $1:10^5$ (*low-metal* experiments). Mixing of the reagents was performed in the glovebox in 100 ml-volume serum bottles. First, 10 mg of elemental sulphur (S^0) was pre-weighed into each bottle. Then, 30 ml of Fe^{2+} solution was aliquoted into each bottle, followed by the addition of 0.5 ml trace metals where applicable. Afterwards, 1.5 ml of HEPES buffer and 1 ml Na_2S were added, followed immediately by sealing of the bottles with butyl rubber stoppers and aluminum crimps. The final mixture contained approximately 3 mM Fe, 6 mM Na_2S, 10 mM S^0 and either 30 µM (*high-metal*) or 30 nM trace metals (*low-metal* experiments). The bottles were incubated statically at 25-80 °C in a dark incubator for up to 14 days. We employed static incubation to better represent environmental conditions in which materials are not consistently well-mixed, such as those found in natural sediments. Final pH was measured to be pH 7 (± 0.1) with a pH probe, indicating the effectiveness of the HEPES buffer.

Polysulphides experiment and analysis

A set of bottles (1 bottle/condition) was prepared to determine the effects of trace metals on polysulphide formation following the protocol above. The only difference was the use of Fe-free NaCl instead of Fe^{2+} solution, which enabled better visualisation of the polysulphide coloration. After incubation, the solutions were sub-sampled, centrifuged at 20,000 x *g* for 2 minutes, and 200 µL of the supernatants were pipetted into a 96-well plate. Absorption was determined via UV-VIS spectroscopy from 250-550 nm, using the same experimental solution without Fe, S and trace metals as a blank.

Mineralogical analyses

Set-1 experiments were completely harvested (i.e., sacrificial sampling) for X-ray diffraction (XRD) and scanning electron microscopy (SEM). Initial attempts to collect the precipitates quantitatively via centrifugation or 0.22 µm filtration were unsuccessful due to the colloidal nature of the precipitates. Hence, aggregation and settling of the precipitates were first induced by adding 3 mL of anoxic 5 M NaCl, followed by incubation at 4 °C overnight. The overlying solution was carefully removed by pipetting. The precipitates were pooled into 1.5 mL tubes by repeated centrifugation at 2,000 x *g* for 5 minutes. The pellets were then washed 3x with 100 % ethanol (preventing colloidal behaviour) before resuspension to 1 mL in anoxic H_2O. An aliquot of ~800 µL was dried as a thin film onto glass slides for XRD analysis. The XRD patterns were collected using a Rigaku Miniflex II equipped with a Cu Kα source from 10-60° 2θ angle with a step size of 0.05° and a scan speed of 0.5°/min, totalling a collection time of 1 h 45 min. The remaining samples were diluted to 10 mL in anoxic H_2O and stored in sealed serum bottles for ~2 years prior to SEM analyses.

Aliquots of *Set-2* experiments were sub-sampled (repetitive sampling) for micro-XRD and SEM. For micro-XRD, around 5 mL was sampled, aggregation and settling induced by the addition of 5 M NaCl (1:10 NaCl:sample ratio) as before, washed 3x in ethanol and finally dried in the glovebox. Micro-XRD patterns of the dried pellets were collected on a Bruker's D8 Discover GADDS XRD2 equipped with a Co Kα source from 5.6-69.1° 2θ angle with a step size of 0.05° and a scan speed of 0.265°/sec, totalling 4 minutes of scanning time (Berthold *et al.*, 2009). For all XRD analyses throughout this study, samples were transferred from the glovebox to the instrument within air-tight containers. Exposure to air was unavoidable during analysis. However, oxidation and transformation of dried Fe sulphides is not expected within the scanning times employed in this study (Boursiquot *et al.*, 2001).

For SEM analysis of both experimental sets, aliquots (50 uL) of the samples were placed directly onto carbon adhesive tabs attached to aluminium stubs. Excess solution was allowed to air-dry overnight within an anaerobic chamber. Once dry, the samples were removed from the glovebox, immediately coated with an 8 nm-thick deposition of gold or platinum using a BAL-TEC™ SCD 005 sputter coater and imaged within the same day. The precipitates were characterised using a Zeiss Crossbeam 550L Scanning Electron Microscope (SEM) equipped with an Oxford Instrument Energy Dispersive Spectrometer (EDS). All micrographs were taken in Secondary Electron (SE) mode with an accelerating voltage of 2 kV. An additional subset of samples was dissolved in 6 M HCl for 10 minutes before SEM imaging to differentiate between HCl-soluble minerals (FeS_{am}, mackinawite, greigite) and HCl-insoluble mineral (pyrite).

The relative XRD signal intensities of pyrite/greigite – a proxy for the extent of pyrite formation – were determined by dividing the height of the main pyrite signal at 33° 2θ with the greigite signal at 30° 2θ (Cu Kα). This approach is only valid when mackinawite is absent, as it also contributes to the 30° signal. Furthermore, this approach does not consider crystallinity variation, which can cause signal broadenings that decrease peak heights. Analyses of duplicate bottles of *no-metals* and *low-metal* Co *Set 1* experiments indicated an error of 0.25 and 0.23, respectively. We conservatively assumed an error of ± 0.25 for all experiments.

SI Discussion

Calculation of pyrite formation rates and potential effects of H_2

For *Set-1* experiments, we used the Match! Software (https://www.crystalimpact.com/match/) to semi-quantitatively obtain the relative abundance of pyrite over greigite at day 14 in the presence of various trace metals. With pyrite's relative abundance of 55-78 % and initial Fe concentration of 3 mM, we calculated formation rates of 1.5-1.9 x 10^{-9} mol/L/s.

For *Set-2* experiments, pyritisation was complete within 3 days and earlier time points were not measured. We therefore calculated a minimum formation rate of 1.2 x 10^{-8} mol/L/s. Hence, *Set-2* experiments exhibited at least 10 times faster pyrite formation than *Set-1* experiments.

In our study, pyrite forms via two parallel pathways:

H_2S pathway:

$$FeS_{aq} + H_2S \rightarrow FeS_2 + H_2 \quad (1)$$

Polysulphide pathway:

$$H_2S + S^0 \rightarrow S_2^{2-} + 2\,H^+ \quad (2)$$

$$FeS_{aq} + S_2^{2-} \rightarrow FeS_2 + S^{2-} \quad (3)$$

Pyritisation via the polysulphide pathway is more important in our study given the presence of S^0 and limited $H_2S_{(aq)}$ from the speciation of $H_2S_{(aq)}/HS^-$ at pH 7 (Mansor and Fantle, 2019). The range of the rate in this study of 10^{-9} to 10^{-8} mol/L/s is similar to those of the 80 °C experiments of Mansor and Fantle (2019) and room temperature pyritisation via the ferric-hydroxide-surface (FHS) pathway (Wan *et al.*, 2017). It is however slightly faster than average rates determined from marine sediments (compiled in Mansor and Fantle, 2019). The relative importance of different pyrite formation pathways in various environments is an open question. Peiffer *et al.*, (2015) noted that the FHS pathway operates at high Fe(III)/S(-II) ratio such as in freshwater systems or at various sediment-water interfaces where sulphide concentration is low, while the polysulphide/H_2S pathways tend to operate deeper in the subsurface in environments rich with sulphate and organic matter that promote microbial sulphate reduction. A recent study noted that the FHS pathway could still operate in deeper sediments under high burial rates (Liu *et al.*, 2021). Hence, the mode of pyrite growth in our study could be applicable to nature given the similarities in the observed rates.

To explore how H_2 can affect pyrite formation via the polysulphide pathway in experimental setups, we first calculated the aqueous concentration of H_2 at equilibrium with 3 % H_2 (1 bar) in the glovebox based on Henry's Law (Sander, 2015) to be 23 µM. We then calculated the Eh of different redox couples in Phreeqc using Minteq database version 4 under the specified experimental condition (pH 7, 3 mM Fe^{2+}, 6 mM Na_2S, 20 mM NaCl, varying $H_{2(aq)}$). The S(-2)/S(6) redox couple has an Eh of -209 mV. The Eh of the H(0)/H(1) redox couple decreases from -203 to -361 mV from negligible concentration to 23 µM $H_{2(aq)}$. Previous studies have noted that pyrite formation is faster under more oxidising conditions (Benning *et al.*, 2000; Butler and Rickard, 2000; Rickard and Luther, 2007) and that different glovebox gas compositions affected whether FeS_{am} or crystalline mackinawite was formed (Csákberényi-Malasics *et al.*, 2012). Rickard and Luther (2007) noted that Eh variations between -200 to -361 mV could greatly affect polysulphide speciation and pyrite supersaturation state at near-neutral pH. Hence, even small quantities of H_2 have the potential to decrease Eh and to slow down pyrite formation.

Disparities in how trace metals affected pyrite formation kinetics

In our *Set-1* experiments, XRD analyses suggested that all tested trace metals (Mo, Ni, Cu, Zn, Co) accelerated pyrite formation relative to when no trace metals were added (**Fig. 1b**). These observations are consistent with many studies (**Table S-1**). However, several disparities exist.

First, Swanner *et al.*, (2019) showed that Co and Ni inhibited pyrite formation at relatively high trace metal to Fe ratios (0.002-0.007 versus 10^{-5} in this study). They synthesised pyrite by reacting 33 mM of dried mackinawite (co-precipitated with Ni or Co to a final concentration of ~0.16 mM in the mixture) with 50 mg of S^0 in pH 6 phthalate buffer for 2 weeks at 65 °C. The final solution volume was not specified – therefore, the total S/Fe ratio is unclear. It was suggested that Co and Ni incorporation into mackinawite increased the mineral's crystallinity, making it less susceptible to dissolution-reprecipitation reactions towards pyrite formation (Baya *et al.*, 2021; Ikogou *et al.*, 2017). Given that we utilised much lower trace metal to Fe ratios, it is likely that the FeS_{am} formed in our experiments were not so affected by this increase in crystallinity. Other studies that tested Ni observed similar accelerating effects as in our study (Morin *et al.*, 2017; Baya *et al.*, 2021; 2022), attributed to the formation of Ni-rich nanoparticles that acted as nuclei for pyrite formation. Those studies did employ similar trace metal to Fe ratios as Swanner *et al.* (2019), but pyrite synthesis was achieved at a pH of 5.5, wherein NiS is one orders of magnitude less soluble than at pH 6 (Mansor *et al.*, 2019). Hence, the formation of NiS that can act as nuclei for pyrite formation becomes more likely under the acidic condition employed in those studies.

The mechanism of how Co can accelerate pyrite formation is less clear than for Ni. Our study is the first to show that Co actually facilitates more polysulphide formation compared to other trace metals tested (**Fig. 3**). A previous study showed that Co substitutes easily into FeS and that the crystallinity of Co-substituted FeS decreases with higher Co content (Mansor *et al.*, 2020), in contrast to what Swanner *et al.*, (2019) observed. We hypothesize that in our current study, the low Co content did not greatly affect the crystallinity of FeS_{am} while it simultaneously facilitated polysulphide formation.

Next, Baya *et al.*, (2022) showed that Mo inhibited pyrite formation at trace metal to Fe ratios of 0.005, which is higher than the ratio of 10^{-5} in this study. They synthesised pyrite by reacting 75 mM aqueous $FeCl_3$ with 75 mM Na_2S at pH 5.5 for up to 129 days at room temperature. They proposed that the formation of colloidal Fe-Mo-S clusters inhibits pyrite formation by slowing down the interaction between polysulphides and Mo-free FeS_x clusters. We hypothesize that the difference in synthesis pH affects the formation of colloidal Fe-Mo-S clusters (Vorlicek *et al.*, 2018) and subsequently how Mo influence pyrite formation. At our experimental pH of 7 and relatively low Mo concentration, less colloidal Fe-Mo-S clusters are expected. Hence, Mo(VI) could function as an oxidant to accelerate pyrite formation at near-neutral pH, consistent with other studies (Mansor and Fantle, 2019; Miller *et al.*, 2020).

Supplementary Tables

Table S-1 Summary of experiments that studied the influence of trace metals on pyrite formation.

Metal	Initial metal/Fe molar ratio	Influence on precipitation rate	Influence on morphology	Synthesis conditions	Proposed mechanism(s)	Reference
As (III)	0.001	Inhibit	?	50 mM $FeCl_3$ + 50 mM Na_2S at pH 5.2-5.8 for 9 weeks at room temperature	Sorption to FeS/pyrite, passivation by As_2S_3, interference of polysulphide formation by forming As-(poly)sulphide complexes	(Baya *et al.*, 2021)
As (III)	10^{-7} to 10	Inhibit	?	9 mM freeze-dried FeS + 18 mM H_2S + Ti(III) citrate in pH 6 phosphate buffer		(Wolthers *et al.*, 2007)
As (III)	0.005	Inhibit	?*	75 mM $FeCl_3$ + 75 mM Na_2S at pH 5.5 for 129 days at room temperature		(Baya *et al.*, 2022)
As(V)	10^{-5} to 10	Inhibit	?	9 mM freeze-dried FeS + 18 mM H_2S + Ti(III) citrate in pH 6 phosphate buffer		(Wolthers *et al.*, 2007)
Co	0.007	Inhibit	?	33 mM dried mackinawite + 50 mg S^0 in pH 6 phthalate buffer for 2 weeks at 65°C. Final solution volume not specified.	Co incorporation increased mackinawite's crystallinity, making it less susceptible to dissolution-reprecipitation reactions (proposed by Baya *et al.*, 2021)	(Swanner *et al.*, 2019)
Co	0.005	Accelerate	?*	75 mM $FeCl_3$ + 75 mM Na_2S at pH 5.5 for 129 days at room temperature	-	(Baya *et al.*, 2022)
Co	0.11	No data	Same shape but smaller size	100 mM FeS + 100 mM polysulphides for 12 hours at 160°C	-	(Lin *et al.*, 2022)

Table S-1 continued Summary of experiments that studied the influence of trace metals on pyrite formation.

Metal	Initial metal/Fe molar ratio	Influence on precipitation rate	Influence on morphology	Synthesis conditions	Proposed mechanism(s)	Reference
Co	10^{-5}	Accelerate	No effect	3 mM Fe^{2+} + 6 mM Na_2S + 10 mM S^0 in pH 7 HEPES buffer for 2 weeks at 80°C	Facilitation of polysulphide formation / acceleration of nucleation	*This study*
Cu	10^{-5}	Accelerate	No effect	3 mM Fe^{2+} + 6 mM Na_2S + 10 mM S^0 in pH 7 HEPES buffer for 2 weeks at 80°C	Facilitation of polysulphide formation / acceleration of nucleation	*This study*
Cu	0.005	Accelerate	?*	75 mM $FeCl_3$ + 75 mM Na_2S at pH 5.5 for 129 days at room temperature	-	(Baya *et al.*, 2022)
Cu	0.1-3.5	Inhibit	-	1:3 Fe:S ratio sonicated for 15 min in diethanolamine and ethanol, then heated for 18 h at 100°C	Enhanced crystallinity and stabilisation of mackinawite by Cu; formation of secondary Cu-Fe mixed phases	(Zavašnik *et al.*, 2014)
Mo	0.00003 to 0.03	Accelerate	?	3 mM Fe^{2+} + 6 mM Na_2S + 10 mM S^0 in pH 7 HEPES buffer for 1 week at 80°C	-	(Mansor and Fantle, 2019)
Mo	0.005 to 0.05	Accelerate	?	60 mg mackinawite/greigite mixture (~135 mM Fe) heated in H_2O for 9 minutes from 80-200°C	Mo(VI) stabilises greigite and accelerates pyrite formation by acting as an oxidant, becoming reduced to Mo(IV) in the process.	(Miller *et al.*, 2020)
Mo	10^{-5}	Accelerate	No effect	3 mM Fe^{2+} + 6 mM Na_2S + 10 mM S^0 in pH 7 HEPES buffer for 2 weeks at 80°C		*This study*
Mo	0.005	Inhibit	?*	75 mM $FeCl_3$ + 75 mM Na_2S at pH 5.5 for 129 days at room temperature	Formation of colloidal Fe-Mo-S clusters slows down interaction of polysulphides with FeS_x clusters	(Baya *et al.*, 2022)

Table S-1 continued Summary of experiments that studied the influence of trace metals on pyrite formation.

Metal	Initial metal/Fe molar ratio	Influence on precipitation rate	Influence on morphology	Synthesis conditions	Proposed mechanism(s)	Reference
Mn	0.005	Accelerate	?*	75 mM $FeCl_3$ + 75 mM Na_2S at pH 5.5 for 129 days at room temperature	-	(Baya *et al.*, 2022)
Mn	0.11	No data	No effect	100 mM FeS + 100 mM polysulphides for 12 hours at 160 °C	-	(Lin *et al.*, 2022)
Ni	10^{-5}	Accelerate	No effect	3 mM Fe^{2+} + 6 mM Na_2S + 10 mM S^0 in pH 7 HEPES buffer for 2 weeks at 80 °C	Facilitation of polysulphide formation / acceleration of nucleation	*This study*
Ni	0.001	Accelerate	?	50 mM $FeCl_3$ + 50 mM Na_2S at pH 5.2-5.8 for 9 weeks at room temperature	Ni accelerated pyrite nucleation	(Baya *et al.*, 2021)
Ni	0.01	Accelerate	?	50 mM $FeCl_3$ + 50 mM Na_2S at pH 5.2-5.8 for 2 weeks at room temperature	Ni accelerated pyrite nucleation	(Morin *et al.*, 2017)
Ni	0.005	Accelerate	?*	75 mM $FeCl_3$ + 75 mM Na_2S at pH 5.5 for 129 days at room temperature	Ni accelerated pyrite nucleation	(Baya *et al.*, 2022)
Ni	0.11	No data	Smaller size and shape change from cubic to octahedral	100 mM FeS + 100 mM polysulphides for 12 hours at 160 °C	-	(Lin *et al.*, 2022)
Ni	0.002	Inhibit	?	33 mM dried mackinawite + 50 mg S^0 in pH 6 phthalate buffer for 2 weeks at 65 °C. Final solution volume not specified.	Ni incorporation increased mackinawite's crystallinity, making it less susceptible to dissolution-reprecipitation reactions (proposed by Baya et al., 2021)	(Swanner *et al.*, 2019)

Table S-1 continued Summary of experiments that studied the influence of trace metals on pyrite formation.

Metal	Initial metal/Fe molar ratio	Influence on precipitation rate	Influence on morphology	Synthesis conditions	Proposed mechanism(s)	Reference
Se	0.005	Accelerate	?*	75 mM $FeCl_3$ + 75 mM Na_2S at pH 5.5 for 129 days at room temperature	-	(Baya *et al.*, 2022)
V	0.005	Inhibit	?*	75 mM $FeCl_3$ + 75 mM Na_2S at pH 5.5 for 129 days at room temperature	-	(Baya *et al.*, 2022)
Zn	10^{-5}	Accelerate	No effect	3 mM Fe^{2+} + 6 mM Na_2S + 10 mM S^0 in pH 7 HEPES buffer for 2 weeks at 80 °C	Facilitation of polysulphide formation / acceleration of nucleation	*This study*
Zn	0.005	Accelerate	?*	75 mM $FeCl_3$ + 75 mM Na_2S at pH 5.5 for 129 days at room temperature	-	(Baya *et al.*, 2022)

*Electron microscopy images showed increasing sizes in the < 1 μm size range in the order of As < Mo < Ni < Co < Zn < Se, but corresponding data on trace metal-free pyrite are not available

Table S-2 Differences between *Set-1* and *Set-2* experiments.

	Set-1	***Set-2***
Location **Year**	University of Texas at El Paso 2019	University of Tuebingen 2022
Experimental design	Sacrificial sampling. *No-metals* and *low-metals* experiments from 25-80 °C	Repetitive sampling. *No-metals*, *low-metal* Co, *high-metals* and Polysulphide experiments at 80 °C
Glovebox and headspace	CoyLab, 97% N_2 - 3% H_2	MBraun, 100% N_2
XRD	Thin film on glass slides, Rigaku Miniflex II, Cu Kα source, 1 h 45 min collection time	Dried pellets, Bruker's D8 Discover GADDS XRD2, Co Kα source, 240 seconds collection time
Storage details before SEM	~2 years in anoxic water at ambient temperature	< 2 weeks in anoxic water at ambient temperature
Reagents	$(NH_4)_2Fe(SO_4)_2{\cdot}6H_2O$ $Na_2S.9H_2O$ S^0; Alfa Aesar product #10785 $CoCl_2{\cdot}6H_2O$ $CuCl_2{\cdot}2H_2O$ $Na_2MoO_4{\cdot}2H_2O$ $NiCl_2{\cdot}6H_2O$ $ZnCl_2$	$FeSO_4.7H_2O$ $Na_2S.9H_2O$ S^0; Sigma Aldrich product #13803 $Co(NO_3)_2{\cdot}6H_2O$ $CuCl_2{\cdot}2H_2O$ $Na_2MoO_4{\cdot}2H_2O$ $NiCl_2{\cdot}6H_2O$ $ZnCl_2$

Table S-3 Summary of experimental conditions, the type of analyses (SEM, magnetism) and the mineralogy as determined by XRD.

Exp	Temp (°C)	Time (days)	Condition	SEM	XRD detection					Magnetism
					FeS_{am}	Greigite	Pyrite	S^0	NaCl	
Set 1	25	7	NoMetal		+			+		NM
	40	7	NoMetal		+			+	+	NM
	40	14	NoMetal	✓	+	+		+	+	NM
	60	7	NoMetal		+	+		+	+	NM
			LowCo		+	+		+		NM
			LowCu		+	+		+		NM
			LowNi		+	+			+	NM
			LowZn		+	+		+	+	NM
	60	14	NoMetal		+	+	+	+	+	NM
			LowCo		+	+	+	+	+	NM
			LowCu		+	+	+		+	NM
			LowNi		+	+	+	+	+	NM
			LowZn		+	+	+		+	NM
	80	14	NoMetal 1	✓		+	+	+		NM
			NoMetal 2			+	+	+		NM
			LowCo 1	✓		+	+	+		NM
			LowCo 2			+	+	+		NM
			LowCu	✓		+	+	+		NM
			LowMo	✓		+	+	+		NM
			LowNi	✓		+	+	+		NM
			LowZn	✓		+	+	+		NM
Set 2	80	0	LowCo	✓	+					-
		3		✓			+			Light
		7		✓			+			Light
		14		✓			+			Light
	80	7	NoMetal			Insufficient sample				Light
			HighCo				+			Light
			HighCu				+			Light
			HighMo			Insufficient sample				Strong
			HighNi			Insufficient sample				Light
			HighZn				+	+		Light
		14	NoMetal	✓			+	+		Light
			HighCo	✓			+	+		Light
			HighCu	✓			+			Light
			HighMo	✓			+	+		Medium
			HighNi	✓			+	+		Light
			HighZn	✓			+			Light

*S^0 and NaCl are residues from the starting materials.

#Magnetic minerals probed with a hand magnet. NM = not measured.

Table S-4 Metadata for SEM images shown in the main text Fig. 2 and Fig. 4

Figure	Exp	Temp (°C)	Time (days)	Condition
2a	*Set 2*	80	0	LowCo
2b	*Set 1*	40	14	NoMe
2c	*Set 1*	40	14	NoMe
2d	*Set 1*	80	14	NoMe
2e	*Set 2*	80	7	HighZn
2f	*Set 1*	80	14	NoMe
2g	*Set 1*	40	14	NoMe
4b	*Set 1*	40	14	NoMe
4d	*Set 2*	80	7	HighZn

Supplementary Figures

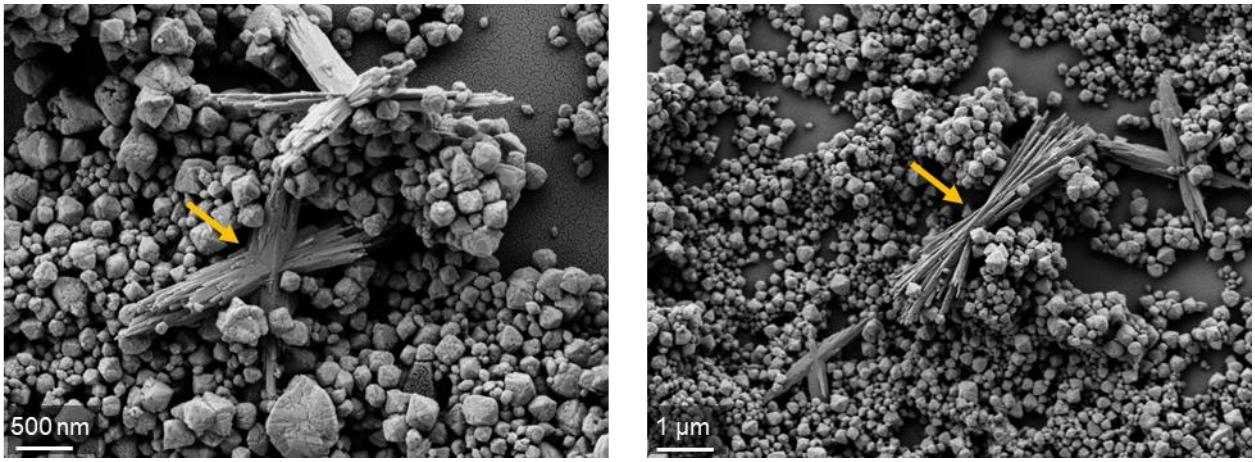

Figure S-1 Representative SEM images of Fe- and oxygen-rich acicular minerals (yellow arrows) in samples from the *Set-2* experiments. The acicular minerals are surrounded by pyrite octahedra of different sizes and degrees of sharp edges. The acicular minerals exhibit twinning features and are reminiscent of goethite (FeOOH), although the mineralogy still needs to be confirmed via techniques such as transmission electron microscopy. Fe(III) (oxyhydr)oxides were not detected with XRD, suggesting low relative abundances.

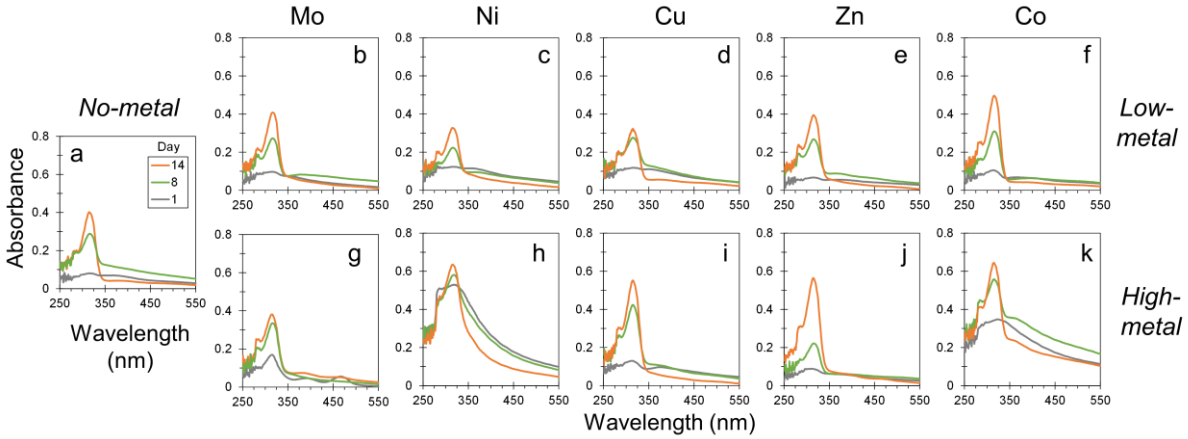

Figure S-2 Absorption spectra of polysulphides in the **(a)** *No-metal* (middle left), **(b-f)** *low-metal* (top row) and **(g-k)** *high-metal* (bottom row) setups at day 1, 8 and 14. Note that (i) enhancements of formation of polysulphides are evident by peaks at 275 and 314 nm, (ii) higher trace metals generally lead to more polysulphide formation, except for Mo, (iii) different trace metals result in different ratios of the 275 and 314 nm peaks, most likely indicating different polysulphide distribution (S_nS^{2-}; different *n* values) and (iv) longer incubation time generally lead to more polysulphides, with the exception of the HighNi setup in which the polysulphide distribution has most likely evolved over time. Individual polysulphide species cannot be identified based on their spectrum alone (Steudel and Chivers, 2019; Kamyshny *et al.*, 2004).

Experiments

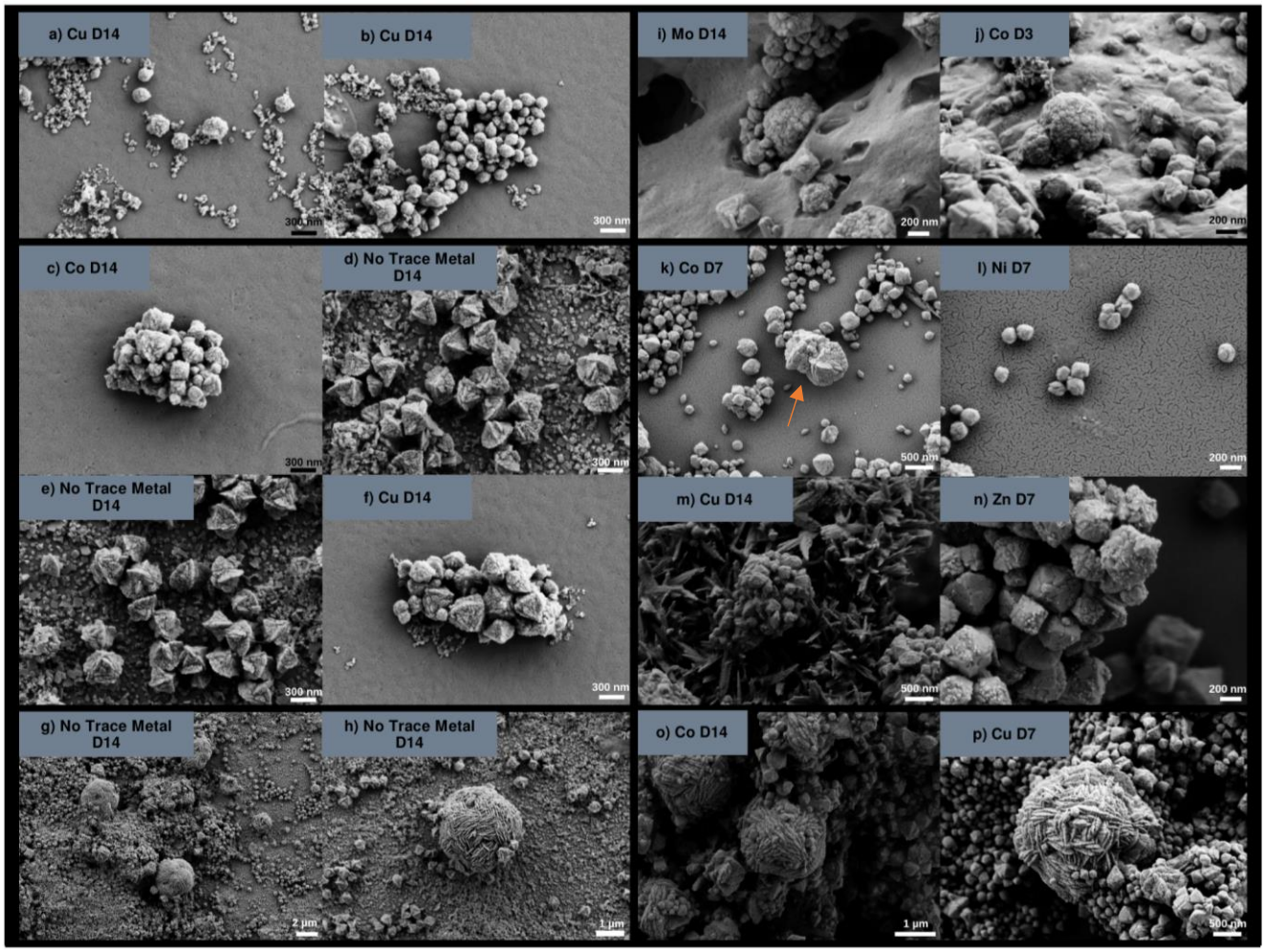

Figure S-3 Comparison of particle morphologies across experiments with varying trace metals. **(a)** Spherical aggregates surrounded by smaller nanoparticles; **(b)** spherical aggregates of varying sizes that are morphing into sharp-edged euhedral crystals; **(c)** agglomerated spherical & octahedral crystals; **(d)** octahedral crystals with extended edges surrounded by smaller tabular nanoparticles; **(e)** octahedral crystals with extended edges surrounded by smaller tabular nanoparticles; **(f)** agglomerated octahedral crystals; **(g)** rose-like crystals surrounded by octahedral crystals and smaller nanoparticles; **(h)** a rose-like crystal surrounded by octahedral crystals and smaller nanoparticles; **(i)** spherical aggregates with octahedral crystals; **(j)** multiple spherical aggregates surrounded by some octahedral crystals; **(k)** a penetration twin (orange arrow) of two octahedral crystals with extended edges surrounded by smaller octahedral crystals; **(l)** spherical aggregates morphing into octahedral crystals; **(m)** agglomerated octahedral crystals; **(n)** multiple octahedral crystals with porous surfaces; **(o)** multiple rose-like

crystals with octahedral crystals in-between; **(p)** rose-like crystal surrounded by octahedral crystals. Note that surface roughness of pyrite has been observed experimentally before but they were not directly linked to growth via particle attachment.

Supplementary Information References

Baya, C., Le Pape, P., Baptiste, B., Brest, J., Landrot, G., Elkaim, E., Noël, V., Blanchard, M., Ona-Nguema, G., Juillot, F., Morin, G. (2021) Influence of trace level As or Ni on pyrite formation kinetics at low temperature. *Geochimica et Cosmochimica Acta* 300, 333–353. https://doi.org/10.1016/j.gca.2021.01.042

Baya, C., Le Pape, P., Baptiste, B., Menguy, N., Delbes, L., Morand, M., Rouelle, M., Aubry, E., Ona-Nguema, G., Noël, V., Juillot, F. (2022) A methodological framework to study the behavior and kinetic influence of V, Mn, Co, Ni, Cu, Zn, As, Se and Mo during pyrite formation via the polysulfide pathway at ambient temperature. *Chemical Geology* 613. https://doi.org/10.1016/j.chemgeo.2022.121139

Benning, L.G., Wilkin, R.T., Barnes, H.L. (2000) Reaction pathways in the Fe-S system below 100^0C. *Chemical Geology* 167, 25–51. https://doi.org/10.1016/S0009-2541(99)00198-9

Berthold, C., Bjeoumikhov, A., Brügemann, L. (2009) Fast XRD^2 microdiffraction with focusing X-Ray microlenses. *Particle and Particle Systems Characterization* 26, 107–111. https://doi.org/10.1002/ppsc.200800038

Boursiquot, S., Mullet, M., Abdelmoula, M., Génin, J.-M., Ehrhardt, J.-J. (2001) The dry oxidation of tetragonal FeS_{1-x} mackinawite. *Physics and Chemistry of Minerals* 28, 600–611. https://doi.org/10.1007/s002690100193

Butler, I.B., Rickard, D. (2000) Framboidal pyrite formation via the oxidation of iron (II) monosulfide by hydrogen sulphide. *Geochimica et Cosmochimica Acta* 64, 2665–2672. https://doi.org/10.1016/S0016-7037(00)00387-2

Csákberényi-Malasics, D., Rodriguez-Blanco, J.D., Kis, V.K., Rečnik, A., Benning, L.G., Pósfai, M. (2012) Structural properties and transformations of precipitated FeS. *Chemical Geology* 294–295, 249–258. https://doi.org/10.1016/j.chemgeo.2011.12.009

Ikogou, M., Ona-Nguema, G., Juillot, F., Le Pape, P., Menguy, N., Richeux, N., Guigner, J.M., Noël, V., Brest, J., Baptiste, B., Morin, G. (2017) Long-term sequestration of nickel in mackinawite formed by *Desulfovibrio capillatus* upon Fe(III)-citrate reduction in the presence of thiosulfate. *Applied Geochemistry* 80, 143–154. https://doi.org/10.1016/j.apgeochem.2017.02.019

Kamyshny, A., Goifman, A., Gun, J., Rizkov, D., Lev, O. (2004) Equilibrium distribution of polysulfide ions in aqueous solutions at 25 degrees C: a new approach for the study of polysulfides' equilibria. *Environmental science & technology* 38, 6633–6644. https://doi.org/10.1021/es049514e

Lin, X., Xia, Y., Wei, G., Zhou, J., Liang, X., Xian, H., Zhu, J., He, H. (2022) Distinct effects of transition metal (cobalt, manganese and nickel) ion substitutions on the abiotic oxidation of pyrite: In view of hydroxyl radical production. *Geochimica et Cosmochimica Acta* 321, 170–183. https://doi.org/10.1016/j.gca.2022.01.026

Liu, J., Antler, G., Pellerin, A., Izon, G., Dohrmann, I., Findlay, A.J., Røy, H., Ono, S., Turchyn, A.V., Kasten, S., Jørgensen, B.B. (2021) Isotopically "heavy" pyrite in marine sediments due to high sedimentation rates and non-steady-state deposition. *Geology* 49, 816–821. https://doi.org/10.1130/G48415.1

Mansor, M., Fantle, M.S. (2019) A novel framework for interpreting pyrite-based Fe isotope records of the past. *Geochimica et Cosmochimica Acta* 253, 39–62. https://doi.org/10.1016/j.gca.2019.03.017

Mansor, M., Winkler, C., Hochella Jr, M.F., Xu, J. (2019) Nanoparticulate nickel-hosting phases in sulfidic environments: Effects of ferrous iron and bacterial presence on mineral

formation mechanism and solid-phase nickel distribution. *Frontiers in Earth Science - Earth and Planetary Materials* 7, 151. https://doi.org/10.3389/feart.2019.00151

Mansor, M., Cantando, E., Wang, Y., Hernandez-Viezcas, J.A., Gardea-Torresdey, J.L., Hochella Jr., M.F., Xu, J. (2020) Insights into the biogeochemical cycling of cobalt: Precipitation and transformation of cobalt sulfide nanoparticles under low-temperature aqueous conditions. *Environmental Science and Technology* 54, 5598–5607. https://doi.org/10.1021/acs.est.0c01363

Miller, N., Dougherty, M., Du, R., Sauers, T., Yan, C., Pines, J.E., Meyers, K.L., Dang, Y.M., Nagle, E., Ni, Z., Pungsrisai, T. (2020) Adsorption of tetrathiomolybdate to iron sulfides and its impact on iron sulfide transformations. *ACS Earth and Space Chemistry* 4, 2246–2260. https://doi.org/10.1021/acsearthspacechem.0c00176

Morin, G., Noël, V., Menguy, N., Brest, J., Baptiste, B., Tharaud, M., Ona-Nguema, G., Ikogou, M., Viollier, E., Juillot, F. (2017) Nickel accelerates pyrite nucleation at ambient temperature. *Geochemical Perspectives Letters* 6–11. https://doi.org/10.7185/geochemlet.1738

Peiffer, S., Behrends, T., Hellige, K., Larese-Casanova, P., Wan, M., Pollok, K. (2015) Pyrite formation and mineral transformation pathways upon sulfidation of ferric hydroxides depend on mineral type and sulfide concentration. *Chemical Geology* 400, 44–55. https://doi.org/10.1016/j.chemgeo.2015.01.023

Rickard, D., Luther, G.W. (2007) Chemistry of iron sulfides. *Chemical Reviews* 107, 514–562. https://doi.org/10.1021/cr0503658

Sander, R. (2015) Compilation of Henry's law constants (version 4.0) for water as solvent. *Atmospheric Chemistry and Physics* 15, 4399–4981. https://doi.org/10.5194/acp-15-4399-2015

Steudel, R., Chivers, T. (2019) The role of polysulfide dianions and radical anions in the chemical, physical and biological sciences, including sulfur-based batteries. *Chemical Society Reviews* 48, 3279–3319. https://doi.org/10.1039/C8CS00826D

Swanner, E.D., Webb, S.M., Kappler, A. (2019) Fate of cobalt and nickel in mackinawite during diagenetic pyrite formation. *American Mineralogist* 104, 917–928. https://doi.org/10.2138/am-2019-6834

Vorlicek, T.P., Helz, G.R., Chappaz, A., Vue, P., Vezina, A., Hunter, W. (2018) Molybdenum burial mechanism in sulfidic sediments: Iron-sulfide pathway. *ACS Earth and Space Chemistry* 2, 565–576. https://doi.org/10.1021/acsearthspacechem.8b00016

Wan, M., Schröder, C., Peiffer, S. (2017) Fe(III):S(-II) concentration ratio controls the pathway and the kinetics of pyrite formation during sulfidation of ferric hydroxides. *Geochimica et Cosmochimica Acta* 217, 334–348. https://doi.org/10.1016/j.gca.2017.08.036

Wolthers, M., Butler, I.B., Rickard, D. (2007) Influence of arsenic on iron sulfide transformations. *Chemical Geology* 236, 217–227. https://doi.org/10.1016/j.chemgeo.2006.09.010

Zavašnik, J., Stanković, N., Arshad, S.M., Rečnik, A. (2014) Sonochemical synthesis of mackinawite and the role of Cu addition on phase transformations in the Fe-S system. *Journal of Nanoparticle Research* 16. https://doi.org/10.1007/s11051-013-2223-z